



**HAL**  
open science

## Tailoring the Plasticity of Topologically Close-packed Phases via the Crystals' Fundamental Building Blocks

Wei Luo, Zhuocheng Xie, Siyuan Zhang, Julien Guéno­lé, Pei-ling Sun, Arno Meingast, Amel Alhassan, Xuyang Zhou, Frank Stein, Laurent Pizzagalli, et al.

### ► To cite this version:

Wei Luo, Zhuocheng Xie, Siyuan Zhang, Julien Guéno­lé, Pei-ling Sun, et al.. Tailoring the Plasticity of Topologically Close-packed Phases via the Crystals' Fundamental Building Blocks. *Advanced Materials*, 2023, pp.2300586. 10.1002/adma.202300586 . hal-04083174v2

**HAL Id: hal-04083174**

**<https://hal.science/hal-04083174v2>**

Submitted on 3 May 2023

**HAL** is a multi-disciplinary open access archive for the deposit and dissemination of scientific research documents, whether they are published or not. The documents may come from teaching and research institutions in France or abroad, or from public or private research centers.

L'archive ouverte pluridisciplinaire **HAL**, est destinée au dépôt et à la diffusion de documents scientifiques de niveau recherche, publiés ou non, émanant des établissements d'enseignement et de recherche français ou étrangers, des laboratoires publics ou privés.

# Tailoring the Plasticity of Topologically Close-Packed Phases via the Crystals' Fundamental Building Blocks

Wei Luo, Zhuocheng Xie,\* Siyuan Zhang,\* Julien Guérolé, Pei-Ling Sun, Arno Meingast, Amel Alhassan, Xuyang Zhou, Frank Stein, Laurent Pizzagalli, Benjamin Berkels, Christina Scheu, and Sandra Korte-Kerzel\*

Brittle topologically close-packed precipitates form in many advanced alloys. Due to their complex structures, little is known about their plasticity. Here, a strategy is presented to understand and tailor the deformability of these complex phases by considering the Nb–Co  $\mu$ -phase as an archetypal material. The plasticity of the Nb–Co  $\mu$ -phase is controlled by the Laves phase building block that forms parts of its unit cell. It is found that between the bulk C15–NbCo<sub>2</sub> Laves and Nb–Co  $\mu$ -phases, the interplanar spacing and local stiffness of the Laves phase building block change, leading to a strong reduction in hardness and stiffness, as well as a transition from synchroshear to crystallographic slip. Furthermore, as the composition changes from Nb<sub>6</sub>Co<sub>7</sub> to Nb<sub>7</sub>Co<sub>6</sub>, the Co atoms in the triple layer are substituted such that the triple layer of the Laves phase building block becomes a slab of pure Nb, resulting in inhomogeneous changes in elasticity and a transition from crystallographic slip to a glide-and-shuffle mechanism. These findings open opportunities to purposefully tailor the plasticity of these topologically close-packed phases in the bulk by manipulating the interplanar spacing and local shear modulus of the fundamental crystal building blocks at the atomic scale.

## 1. Introduction

New materials with superior strength, ductility, and high temperature capability are at the heart of future developments to meet challenges in mobility, energy conversion, and sustainability. In knowledge-based development of structural materials, we commonly design and manipulate the materials' internal (micro)structures at several length scales to control the physical mechanisms governing deformation. This strategy has been particularly successful in the invention of advanced high-strength steels outperforming those used over previous decades within years by an order of magnitude in strength and deformability.<sup>[1]</sup> While the origin of mechanical strength, toughness, and creep resistance is well studied in metals, very little is known about the properties of intermetallics, despite their wide use as reinforcement phases and their sheer number and variability.<sup>[2]</sup> If we were

W. Luo, Z. Xie, P.-L. Sun, S. Korte-Kerzel  
Institute for Physical Metallurgy and Materials Physics  
RWTH Aachen University  
Kopernikusstraße 14, 52074 Aachen, Germany  
E-mail: xie@imm.rwth-aachen.de; korte-kerzel@imm.rwth-aachen.de

S. Zhang, X. Zhou, F. Stein, C. Scheu  
Max-Planck-Institut für Eisenforschung GmbH  
Max-Planck-Straße 1, 40237 Düsseldorf, Germany  
E-mail: siyuan.zhang@mpie.de

J. Guérolé  
CNRS  
Arts et Métiers ParisTech  
Université de Lorraine  
LEM3, Metz 57070, France

J. Guérolé  
Labex Damas  
Université de Lorraine  
Metz 57070, France  
A. Meingast  
Thermo Fisher Scientific  
De Schakel 2, Eindhoven 5651 GH, The Netherlands

A. Alhassan, B. Berkels  
Institute for Advanced Study in Computational Engineering Science  
RWTH Aachen University  
Schinkelstr. 2, 52062 Aachen, Germany

L. Pizzagalli  
Institut Pprime  
CNRS UPR 3346  
Université de Poitiers  
SP2MI  
Boulevard Marie et Pierre Curie, TSA 41123, Poitiers Cedex 9, Poitiers  
86073, France

 The ORCID identification number(s) for the author(s) of this article can be found under <https://doi.org/10.1002/adma.202300586>

© 2023 The Authors. Advanced Materials published by Wiley-VCH GmbH. This is an open access article under the terms of the Creative Commons Attribution License, which permits use, distribution and reproduction in any medium, provided the original work is properly cited.

DOI: 10.1002/adma.202300586

to understand the physical origin of their mechanical properties based on the underlying deformation mechanisms as well as we do now in metals and metallic alloys, we could manipulate their strength and toughness. Predicting and controlling the plasticity of intermetallics is of great interest as we could tailor highly alloyed materials to form only those intermetallics that reinforce but do not introduce damage by brittle cracking.

A large fraction of complex intermetallics can be simplified as an intergrowth of a few simple fundamental units.<sup>[3]</sup> Considering the simple fundamental building blocks of complex intermetallics, rather than entire large unit cells, provides a pathway to unravel the plasticity of complex intermetallics. Their deformation mechanisms depend sensitively on these simpler fundamental building blocks. In particular, it is important to understand how they combine to form the complex structures, how they allow deformation to occur as an ensemble, and how each is affected by changes in chemical composition at the atomic scale of the crystal lattice. Furthermore, the recurrent nature of the few fundamental building blocks<sup>[3]</sup> will allow a transfer of knowledge to a large number of complex phases. Such knowledge would allow us to mine the existing, enormous crystal databases for exceptional phases that could form the basis for future high performance alloys.

The topologically close-packed (TCP) phases are commonly found in superalloys<sup>[4]</sup> but their plasticity is lesser known due to their complex crystal structures. Laves phases are the most common intermetallic compounds with a relatively simple TCP structure formed by stacking of quadruple Laves phase layers which are composed of a kagomé layer and a triple layer.<sup>[5]</sup> The Laves phases have been confirmed to plastically deform via a synchroshear mechanism,<sup>[6]</sup> which consists of two shears in different directions on adjacent atomic planes of the triple layer structural unit. Although synchroshear is geometrically and energetically more favorable than the common crystallographic slip in the Laves phase,<sup>[7]</sup> the motion of the associated synchro-Shockley partial dislocations needs to overcome high energy barriers with the help of thermal activation,<sup>[8]</sup> leading to the intrinsically high strength and brittleness of the Laves phases. The  $\mu$ -phase is a common intermetallic precipitate phase with a complex TCP structure in superalloys<sup>[4a,9]</sup> but our knowledge about its plasticity is still limited. As the  $\mu$ -phase consists of  $\text{NbCo}_2$  Laves phase layers (prototype  $\text{MgCu}_2$ ) interspersed by monoatomic layers of  $\text{Nb}_4\text{Co}_3$  (prototype  $\text{Zr}_4\text{Al}_3$ ),<sup>[10]</sup> as illustrated in **Figure 1**, synchroshear is therefore thought to also occur in the  $\mu$ -phase.<sup>[11]</sup> However, the local atomic environment of the Laves phase building block in the  $\mu$ -phase is different from that in the Laves phases, which may lead to different interplanar spacings, different local stiffnesses of the interatomic bonds, and thus distinct mechanical behavior. Moreover, the  $\mu$ -phase can have a wide composition range and it can be stable at off-stoichiometric compositions where the atomic configurations of the Laves phase building block are substantially modified by the constitutional defects.<sup>[12]</sup> Therefore, we use the  $\mu$ -phase as a model for three reasons: 1) to explore the influence of crystal structure and composition on the mechanical behavior of the fundamental Laves phase building block, 2) to understand the plasticity of the complex but common  $\mu$ -phase itself, and 3) to open up opportunities for controlling the deformation mechanisms and tailoring the mechanical properties of complex TCP phases more generally.

In the present work, we investigated the mechanical properties of the Nb–Co  $\mu$ -phase and the closely related C15– $\text{NbCo}_2$  Laves phase by nanoindentation tests and found that a reduction in both hardness and indentation modulus can be achieved by changing the structure and composition. Furthermore, we revealed how the structure and composition affect the mechanical properties and deformation mechanisms of the Laves phase building block by means of aberration-corrected high-angle annular dark-field scanning transmission electron microscopy (HAADF-STEM) combined with atomic-resolution energy dispersive X-ray spectroscopy (EDS) analysis and density functional theory (DFT) calculations.

## 2. Results and Discussion

### 2.1. Influence of Composition on the Atomic Configurations

In the  $\mu$ -phase, while the large atoms prefer to occupy the positions with high coordination numbers (CNs = 14, 15, and 16), the small atoms tend to occupy the positions with a low CN (CN = 12).<sup>[10]</sup> The stoichiometric composition of the  $\mu$ - $\text{Nb}_6\text{Co}_7$  phase is about 46.2 at% Nb. As the composition deviates from the stoichiometric composition, constitutional defects, such as antisite atoms, are expected in the Nb–Co  $\mu$ -phase.<sup>[12]</sup> In order to study the atomic configurations of the Nb–Co  $\mu$ -phase at off-stoichiometric compositions, the elemental maps of the  $\text{Nb}_{6.4}\text{Co}_{6.6}$  (Figure 1a) and  $\text{Nb}_7\text{Co}_6$  (Figure 1b) alloys (Table S1, Supporting Information) of the Nb–Co  $\mu$ -phase were measured by atomic-resolution EDS analysis. As shown in Figure 1a,b, the positions with high CNs (CN = 14, 15, and 16) are exclusively occupied by large Nb atoms, and the positions in the kagomé layers which have a low CN (CN = 12) are fully occupied by small Co atoms. However, in the middle (CN = 12) of the triple layers, Nb was detected in both the  $\text{Nb}_{6.4}\text{Co}_{6.6}$  and  $\text{Nb}_7\text{Co}_6$  alloys. While both Co and Nb occur in the middle (CN = 12) of the triple layers in the  $\text{Nb}_{6.4}\text{Co}_{6.6}$  alloy (Figure 1a), hardly any Co remains in the middle (CN = 12) of the triple layers in the  $\text{Nb}_7\text{Co}_6$  alloy (Figure 1b). This indicates that, in the Nb-rich Nb–Co  $\mu$ -phase, the excess Nb atoms substitute the Co atoms specifically in the middle of the triple layers. Therefore, as the composition is reversed from  $\text{Nb}_6\text{Co}_7$  to  $\text{Nb}_7\text{Co}_6$ , the general structure of the Nb–Co  $\mu$ -phase (Figure 1c) is preserved but the Co atoms in the triple layers are replaced by Nb atoms, and thus the puckered close-packed Nb–Co–Nb triple layer of the Laves phase building block becomes a slab of pure Nb (Figure 1d).

The interplanar spacing between the basal planes of the middle and the bottom of the triple layer  $d_t$ , and the interplanar spacing between the basal planes of the bottom of the triple layer and kagomé layer  $d_{t-k}$  (Figure 1c), measured from HAADF-STEM images of the  $\text{Nb}_{6.4}\text{Co}_{6.6}$  alloy are  $0.32 \pm 0.02$  and  $1.70 \pm 0.12$  Å, respectively. The respective values of  $d_t$  and  $d_{t-k}$  of the  $\text{Nb}_7\text{Co}_6$  alloy are  $0.43 \pm 0.02$  and  $1.67 \pm 0.08$  Å. These measurements were made using a novel mathematical analysis on STEM images based on variational methods for motif extraction.<sup>[13]</sup> We also investigated the interplanar spacings of the Nb–Co  $\mu$ -phase and the closely related C15– $\text{NbCo}_2$  Laves phase by DFT calculations. As the crystal structure changes from C15– $\text{NbCo}_2$  to  $\mu$ - $\text{Nb}_6\text{Co}_7$ ,  $d_t$  decreases dramatically from 0.481 to 0.272 Å (Table S2, Supporting Information) whereas  $d_{t-k}$  increases from 1.454 to 1.700 Å.

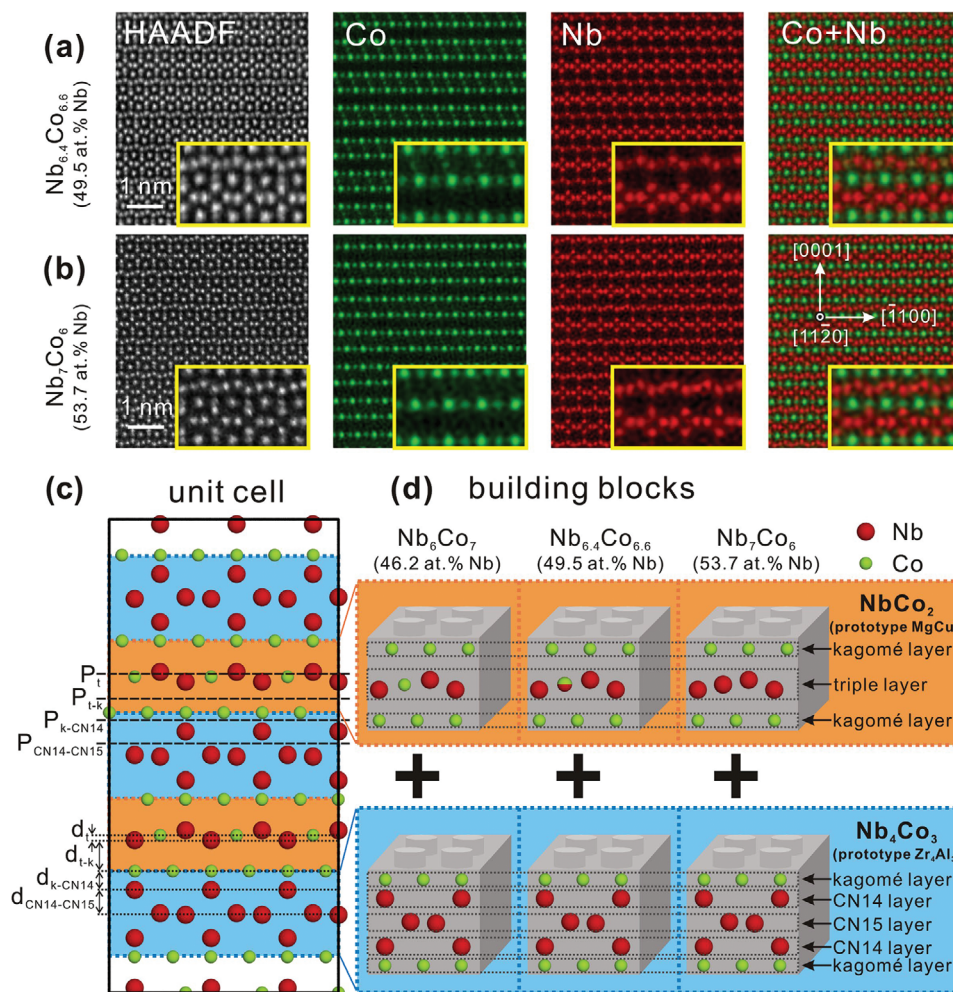


**Figure 1.** a,b) HAADF-STEM images and the corresponding atomic-resolution EDS maps of the  $\text{Nb}_{6.4}\text{Co}_{6.6}$  (a) and  $\text{Nb}_7\text{Co}_6$  (b) alloys showing the distributions of Co and Nb in the Nb–Co  $\mu$ -phase. c,d) Schematics of the  $[11\bar{2}0]$  projection of the Nb–Co  $\mu$ -phase showing the unit cell of  $\mu\text{-Nb}_6\text{Co}_7$  (c) and the stacking of the  $\text{NbCo}_2$  Laves phase and  $\text{Nb}_4\text{Co}_3$  building blocks in  $\mu\text{-Nb}_6\text{Co}_7$ ,  $\mu\text{-Nb}_{6.4}\text{Co}_{6.6}$ , and  $\mu\text{-Nb}_7\text{Co}_6$  (d).  $P_t$ ,  $P_{t-k}$ ,  $P_{k\text{-CN}14}$ , and  $P_{\text{CN}14\text{-CN}15}$  denote the basal plane between the top and middle layers of the triple layer (the plane between middle and bottom layer is equivalent), the basal plane between the bottom of the triple layer and the kagomé layer, the basal plane between the kagomé layer and the CN14 layer, and the basal plane between the CN14 layer and the CN15 layer, respectively.  $d_t$ ,  $d_{t-k}$ ,  $d_{k\text{-CN}14}$ , and  $d_{\text{CN}14\text{-CN}15}$  are the corresponding interplanar spacings.

As the composition of the Nb–Co  $\mu$ -phase changes from  $\text{Nb}_6\text{Co}_7$  to  $\text{Nb}_7\text{Co}_6$ ,  $d_t$  changes from 0.272 to 0.363 Å, while  $d_{t-k}$  remains nearly constant. These DFT calculations are consistent with the results measured from experimental HAADF-STEM images.

## 2.2. Influence of Composition on the Mechanical Response

Nanoindentation tests were performed on the  $\text{Nb}_{6.4}\text{Co}_{6.6}$ ,  $\text{Nb}_{6.9}\text{Co}_{6.1}$ , and  $\text{Nb}_7\text{Co}_6$  alloys to study the influence of composition on the hardness and indentation modulus of the Nb–Co  $\mu$ -phase. As shown in the postmortem scanning electron microscopy (SEM) images (Figure 2a–c), the straight basal slip traces around the indentations reveal that plastic deformation of the Nb–Co  $\mu$ -phase occurs in an anisotropic manner, predominantly by basal slip. In contrast to the hexagonal Laves phase, which can deform plastically by both basal and nonbasal slips

at room temperature,<sup>[14]</sup> the Nb–Co  $\mu$ -phase only shows visible slip traces of nearly exclusively basal slip even in orientations where nonbasal slip is favorable (Figure S1a–d, Supporting Information). When the basal plane is aligned perpendicular to the loading direction, the applied strain is accommodated by pileup without clearly interpretable features of slip at the surface and cracking at the corners.

The hardness (Figure 2d) of the Nb–Co  $\mu$ -phase is lower than that of the C15– $\text{NbCo}_2$  Laves phase. As the Nb content increases, the nanoindentation hardness of the Nb–Co  $\mu$ -phase decreases from  $12.6 \pm 0.6$  GPa at 49.5 at% Nb to  $11.9 \pm 0.3$  GPa at 52.8 at% Nb, and to  $10.9 \pm 0.3$  GPa at 53.7 at% Nb, corresponding to estimates of the macroscopic hardness after Nix and Gao<sup>[15]</sup> of  $10.2 \pm 1.0$  GPa at 49.5 at% Nb to  $9.5 \pm 0.7$  GPa at 52.8 at% Nb, and to  $8.5 \pm 0.8$  GPa at 53.7 at% Nb. The decrease in hardness with increasing Nb content agrees with the composition dependence of critical resolved shear stress for basal slip measured by

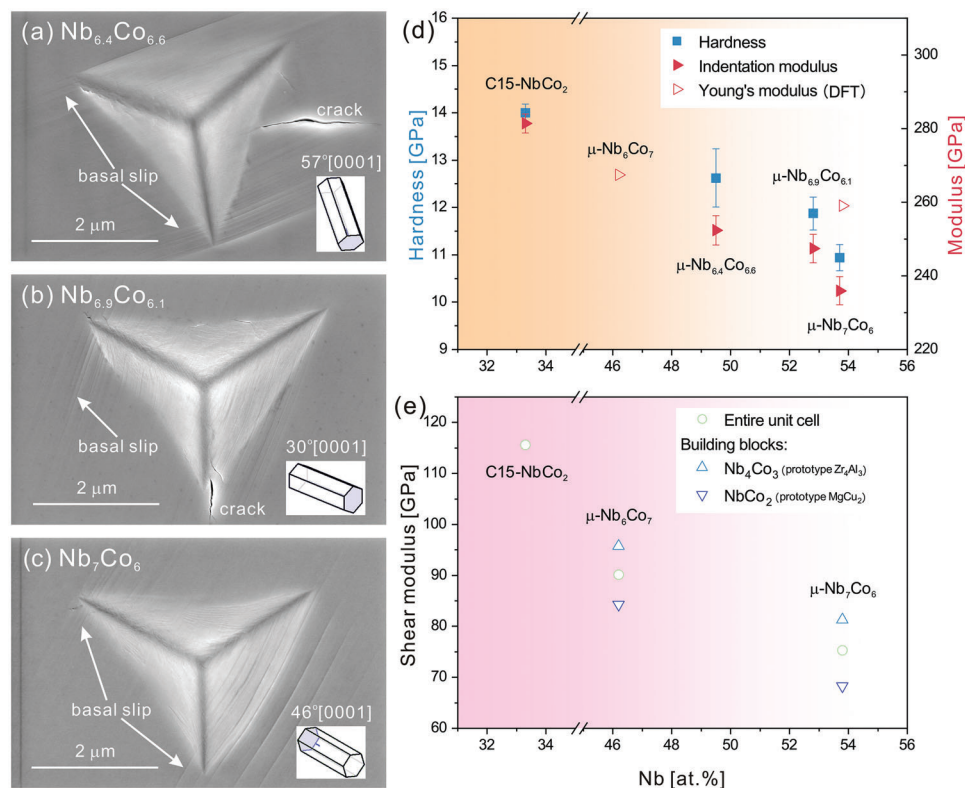


**Figure 2.** a–c) Representative SEM images of indentations of the Nb<sub>6.4</sub>Co<sub>6.6</sub> (a), Nb<sub>6.9</sub>Co<sub>6.1</sub> (b), and Nb<sub>7</sub>Co<sub>6</sub> (c) alloys showing the surface slip traces after indentation tests. The orientations are denoted by the angle between the loading axis and the *c*-axis of the Nb–Co  $\mu$ -phase. Unit cells representing the orientations are inset. d) The composition dependence of hardness and indentation modulus of the Nb–Co  $\mu$ -phase measured by nanoindentation tests as well as the Young's modulus determined by DFT (entire unit cell). e) Calculated basal plane shear moduli of the entire unit cell of C15–NbCo<sub>2</sub>,  $\mu$ -Nb<sub>6</sub>Co<sub>7</sub>, and  $\mu$ -Nb<sub>7</sub>Co<sub>6</sub> and the Nb<sub>4</sub>Co<sub>3</sub> and NbCo<sub>2</sub> building blocks of the two  $\mu$ -phases.

micropillar compression, which indicates an even larger drop to less than a third in critical resolved shear stress on the basal plane.<sup>[16]</sup> The indentation modulus (Figure 2d) shows a similar compositional trend as the hardness. The measured indentation modulus (Figure 2d) of the Nb–Co  $\mu$ -phase is lower than that of the C15–NbCo<sub>2</sub> Laves phase, and it decreases from 253 ± 4 GPa at 49.5 at% Nb to 247 ± 4 GPa at 52.8 at% Nb, and to 236 ± 4 GPa at 53.7 at% Nb. Nanoindentation tests performed in selected grains with different orientations (Figure S2a–i, Supporting Information) reveal that the influence of orientation on the hardness and indentation modulus of the Nb–Co  $\mu$ -phase is negligible.

The elastic properties and elastic anisotropy of  $\mu$ -Nb<sub>6</sub>Co<sub>7</sub> and  $\mu$ -Nb<sub>7</sub>Co<sub>6</sub> were also investigated by DFT calculations. The calculated Young's modulus and shear modulus of  $\mu$ -Nb<sub>7</sub>Co<sub>6</sub> are lower than those of  $\mu$ -Nb<sub>6</sub>Co<sub>7</sub> (Table S3, Supporting Information), which is consistent with the compositional trend of indentation modulus measured from the nanoindentation tests. Similarly, the low elastic anisotropy found in indentation is also predicted by DFT with an anisotropy index of the order of 0.2 (Table S3, Supporting Information). The overall basal plane shear modulus and the respective basal plane shear moduli of the Nb<sub>4</sub>Co<sub>3</sub> and NbCo<sub>2</sub> Laves phase building blocks of the Nb–Co  $\mu$ -phase were calculated and compared with the  $\langle 111 \rangle$  plane shear modulus of the closely related bulk C15–NbCo<sub>2</sub> Laves phase in Figure 2e. The overall basal plane shear modulus of the Nb–Co

$\mu$ -phase is significantly lower than the  $\langle 111 \rangle$  plane shear modulus of the bulk C15–NbCo<sub>2</sub> Laves phase, and it decreases from 90.1 to 75.3 GPa as the composition changes from Nb<sub>6</sub>Co<sub>7</sub> to Nb<sub>7</sub>Co<sub>6</sub>. Moreover, although the shear modulus is isotropic on the basal plane of the Nb–Co  $\mu$ -phase, the basal plane shear moduli of the two building blocks are different. As shown in Figure 2e, the basal plane shear modulus of the NbCo<sub>2</sub> Laves phase building block is lower than that of the Nb<sub>4</sub>Co<sub>3</sub> building block, indicating that the Laves phase building block is more compliant, and thus is more prone to shear straining than the Nb<sub>4</sub>Co<sub>3</sub> building block in the Nb–Co  $\mu$ -phase. The basal plane shear modulus of the Laves phase building block is about 12% and 16% lower than that of the Nb<sub>4</sub>Co<sub>3</sub> building block in  $\mu$ -Nb<sub>6</sub>Co<sub>7</sub> and  $\mu$ -Nb<sub>7</sub>Co<sub>6</sub>, respectively. This suggests that as the composition changes from Nb<sub>6</sub>Co<sub>7</sub> to Nb<sub>7</sub>Co<sub>6</sub>, the elastic inhomogeneity between the two building blocks becomes more pronounced.

### 2.3. Dislocation Structures in Nb<sub>6.4</sub>Co<sub>6.6</sub> and Nb<sub>7</sub>Co<sub>6</sub> Alloys

As shown in the postmortem SEM image (Figure S1b, Supporting Information), the Nb<sub>6.4</sub>Co<sub>6.6</sub> alloy shows a high density of straight basal slip traces around the indentation when indented along the 83° [0001] direction. In order to study the dislocation structures, a transmission electron microscopy (TEM) lamella of

the 83° [0001] indentation of the Nb<sub>6.4</sub>Co<sub>6.6</sub> alloy was prepared. The bright-field TEM image taken with  $g = \bar{1}101$  (Figure S3a, Supporting Information) shows that there are numerous dislocations and several widely extended stacking faults parallel to the basal plane underneath the indentation. When imaged with  $g = 0003$  (Figure S3b, Supporting Information), the defects are out of contrast, which confirms that their Burgers vectors are on the basal plane. As the wide stacking faults start at the top surface and extend to the bottom of the lamella, they are assumed to be grown-in defects. While the contrast of the widely extended stacking faults is well visible and their widths change when the sample is tilted, no contrast of stacking faults between the dislocations can be observed. The dislocations are therefore either full dislocations without dissociation or the dissociation distance is too narrow to be resolved in the bright-field TEM images.

In order to further resolve the structures of the dislocations, we performed aberration-corrected HAADF-STEM imaging. A full dislocation in the Nb<sub>6.4</sub>Co<sub>6.6</sub> alloy is shown in Figure 3a. The closure failure of the Burgers circuit reveals that the imaged core corresponds to a full dislocation with  $b = \frac{1}{3}\langle\bar{2}110\rangle$  lying between the kagomé layer and the triple layer of the NbCo<sub>2</sub> Laves phase building block. While most of the defects imaged in the plastic zone of the indentation were confirmed to be full dislocations with  $b = \frac{1}{3}\langle\bar{2}110\rangle$ , a few partial dislocations bounding stacking faults on the basal plane were also observed. The partial dislocation core and the associated stacking fault in the Nb<sub>6.4</sub>Co<sub>6.6</sub> alloy are shown in Figure 3b. The stacking fault is located in the triple layer of the NbCo<sub>2</sub> Laves phase building block and the stacking sequence of the triple layer changes to the twinned variant in the stacking fault. The closure failure of the Burgers circuit confirms that the partial dislocation has a Burgers vector of  $b = \frac{1}{3}\langle 0\bar{1}10\rangle$ .

In the Nb<sub>7</sub>Co<sub>6</sub> alloy, a high density of straight basal slip traces was observed around the indentation with a loading axis of 46° [0001] (Figure 2c). In the bright-field TEM image from such an indentation, numerous planar defects parallel to the basal plane and bounded by partial dislocations were observed using a two-beam condition with  $g = \bar{1}101$  (Figure S3c, Supporting Information). The planar defects are out of contrast for  $g = 0003$  (Figure S3d, Supporting Information), which confirms that the Burgers vectors of the planar defects in Nb<sub>7</sub>Co<sub>6</sub> alloy are also on the basal plane. The structure of a stacking fault bound by partial dislocations in this sample was also imaged by HAADF-STEM (Figure 3c) along the [11 $\bar{2}$ 0] direction. At the dislocation core, the parallelograms containing triple layers change direction, indicating that the stacking fault is located in the NbCo<sub>2</sub> Laves phase building block. The closure failure of the Burgers circuit around the dislocation core reveals the partial dislocation Burgers vector  $b = \frac{1}{3}\langle\bar{1}100\rangle$ .

#### 2.4. Energetically Favorable Slip Events

In order to reveal the energy paths of crystallographic slip in the Nb–Co  $\mu$ -phase, we calculated the generalized stacking fault energy (GSFE) curves of the crystallographic slip on different basal planes along the  $\frac{1}{3}\langle 11\bar{2}0\rangle$  direction in  $\mu$ -Nb<sub>6</sub>Co<sub>7</sub> (Figure 4a) and  $\mu$ -Nb<sub>7</sub>Co<sub>6</sub> (Figure 4b). The crystallographic slip mechanism<sup>[7a,c]</sup> involves the sliding of one half of a crystal relative to the other half of the crystal on the basal plane along a crystallographic direction

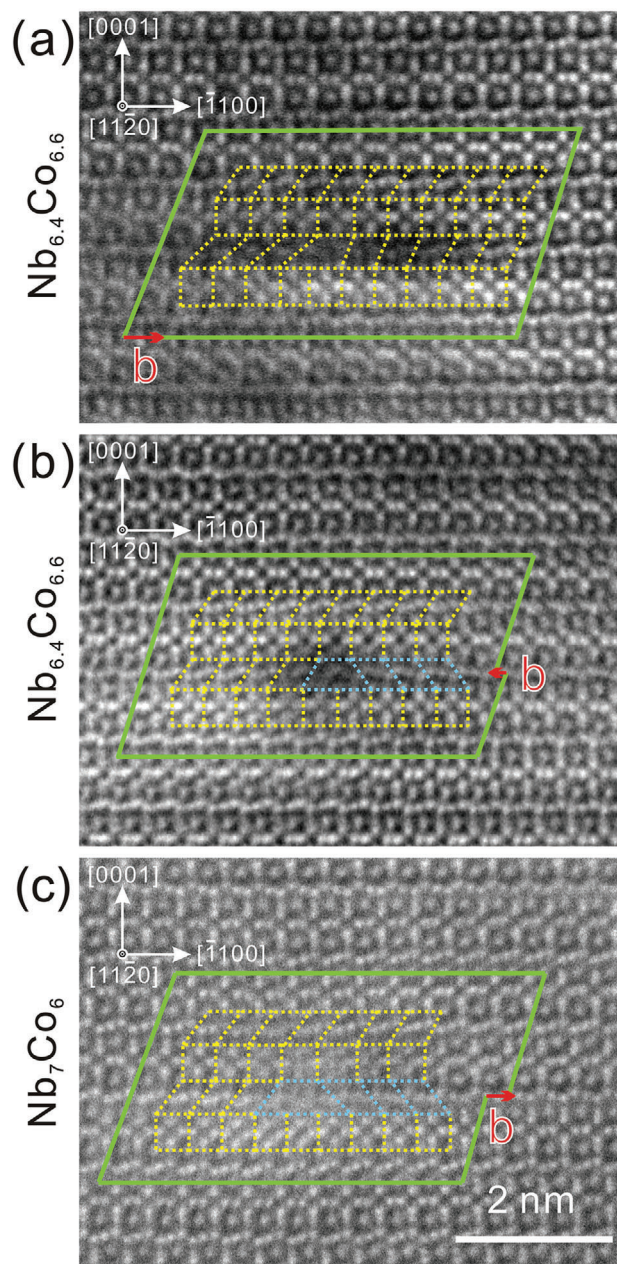


**Figure 3.** Atomic configurations of the defects on the basal plane of the Nb–Co  $\mu$ -phase under an indentation viewed along the [11 $\bar{2}$ 0] axis. a–c) HAADF-STEM images of a full dislocation in the Nb<sub>6.4</sub>Co<sub>6.6</sub> alloy viewed end-on (a), a partial dislocation bounding a stacking fault in the Nb<sub>6.4</sub>Co<sub>6.6</sub> alloy (b), and a partial dislocation bounding a stacking fault in the Nb<sub>7</sub>Co<sub>6</sub> alloy (c). The Burgers vectors marked by red arrows are measured from the closure failures of the green Burgers circuits. The stacking of the building blocks of the Nb–Co  $\mu$ -phase and the stacking faults are outlined using yellow and blue tiles, respectively.

perpendicular to the stacking direction. Among the four possible sets of basal planes  $P_{\text{CN14–CN15}}$ ,  $P_{\text{k–CN14}}$ ,  $P_{\text{t–k}}$ , and  $P_{\text{t}}$ , we find that crystallographic slip on  $P_{\text{t–k}}$  exhibits the lowest energy barrier in both  $\mu$ -Nb<sub>6</sub>Co<sub>7</sub> (Figure 4a) and  $\mu$ -Nb<sub>7</sub>Co<sub>6</sub> (Figure 4b). The GSFE curves of crystallographic slip on  $P_{\text{t–k}}$  along the  $\frac{1}{3}\langle 1100\rangle$

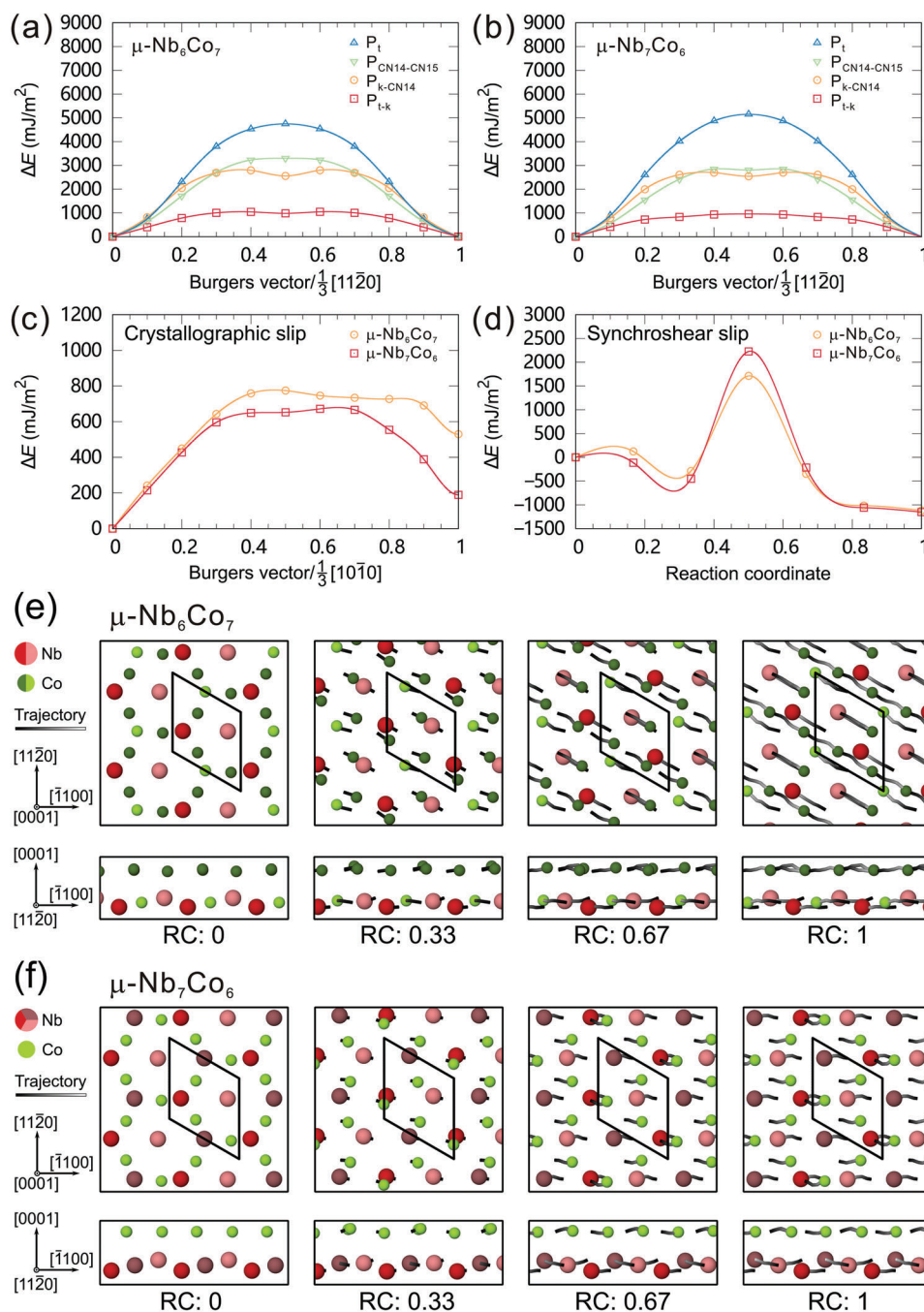


**Figure 4.** Assessment of the slip mechanisms in  $\mu$ -Nb<sub>6</sub>Co<sub>7</sub> and  $\mu$ -Nb<sub>7</sub>Co<sub>6</sub> using DFT. a,b) GSFE curves of the crystallographic slip along the  $\frac{1}{3}[11\bar{2}0]$  direction on different basal planes in  $\mu$ -Nb<sub>6</sub>Co<sub>7</sub> (a) and  $\mu$ -Nb<sub>7</sub>Co<sub>6</sub> (b). c,d) Energy profiles of the crystallographic slip along the  $\frac{1}{3}[10\bar{1}0]$  direction on  $P_{t-k}$  calculated by GSFE (c) and synchroshear calculated using the NEB method (d). e,f) Snapshots of basal slip on  $P_{t-k}$  via the crystallographic slip mechanism in  $\mu$ -Nb<sub>6</sub>Co<sub>7</sub> (e) and via the glide and shuffle mechanism in  $\mu$ -Nb<sub>7</sub>Co<sub>6</sub> (f). Large (colored in different shades of red) and small (colored in green) atoms are Nb and Co atoms, respectively. Trajectories of atoms are colored in a black-gray gradient according to the reaction coordinate.

direction in  $\mu$ -Nb<sub>6</sub>Co<sub>7</sub> and  $\mu$ -Nb<sub>7</sub>Co<sub>6</sub> are given in Figure 4c. The GSFE curve of crystallographic slip on  $P_{t-k}$  along the  $\frac{1}{3}\langle 1100 \rangle$  direction in  $\mu$ -Nb<sub>7</sub>Co<sub>6</sub> shows a lower energy barrier and a more pronounced local minimum than that in  $\mu$ -Nb<sub>6</sub>Co<sub>7</sub>. Crystallographic slip on  $P_{t-k}$  therefore becomes easier and dislocation dissociation

is more likely to occur as the composition of the Nb–Co  $\mu$ -phase changes from Nb<sub>6</sub>Co<sub>7</sub> to Nb<sub>7</sub>Co<sub>6</sub>. Moreover, the Nb–Co  $\mu$ -phase has a lower energy barrier to basal slip on  $P_{t-k}$  than the C15–NbCo<sub>2</sub> Laves phase (Figure S4a, Supporting Information), presumably due to the larger interplanar spacing  $d_{t-k}$  in the Nb–Co

$\mu$ -phase. Therefore, crystallographic slip on  $P_{t-k}$  becomes increasingly more favorable as the Nb–Co TCP phase changes from the Laves C15–NbCo<sub>2</sub> to  $\mu$ -Nb<sub>6</sub>Co<sub>7</sub>, and to  $\mu$ -Nb<sub>7</sub>Co<sub>6</sub>.

In order to explore the minimum energy paths (MEPs) and the associated atomic mechanisms of the basal slip mechanisms other than the classical crystallographic slip in the Nb–Co  $\mu$ -phase, DFT nudged elastic band (NEB) calculations were performed for basal slip on  $P_t$  and  $P_{t-k}$  of the NbCo<sub>2</sub> Laves phase building block. To ensure a constant strain state throughout the NEB calculations, the initial configuration was elastically strained with a shear of a full Burgers vector, which is equivalent to the plastic strain of the final configuration (Figure S5, Supporting Information). The NEB calculations predict that synchroshear is the energetically most favorable slip mechanism on  $P_t$  in both  $\mu$ -Nb<sub>6</sub>Co<sub>7</sub> and  $\mu$ -Nb<sub>7</sub>Co<sub>6</sub> (Figure 4d). The NEB calculations were also performed on  $P_t$  of the C15–NbCo<sub>2</sub> Laves phase for comparison. The computed MEP and the atomic mechanism of basal slip on the  $P_t$  of the C15–NbCo<sub>2</sub> Laves phase are also associated with the synchroshear mechanism (Figure S4b,c, Supporting Information), which agrees with previous *ab initio*<sup>[7a]</sup> and atomistic simulations.<sup>[7c,8a]</sup> The energy barrier to synchroshear in the Nb–Co  $\mu$ -phase (Figure 4d) is much higher than that in the C15–NbCo<sub>2</sub> Laves phase (Figure S4b, Supporting Information) presumably due to the reduced interplanar spacing  $d_t$ , and the energy barrier to synchroshear in the Nb–Co  $\mu$ -phase increases dramatically from 1999.7 to 2677.8 mJ m<sup>-2</sup> as the composition changes from Nb<sub>6</sub>Co<sub>7</sub> to Nb<sub>7</sub>Co<sub>6</sub>.

The synchroshear mechanism is less sensitive to the applied shear strain owing to the thermally activated nature of the kink-pair nucleation and propagation of synchro-Shockley dislocations.<sup>[8a]</sup> By contrast, the computed MEPs show that the energy barriers to basal slip on  $P_{t-k}$  in  $\mu$ -Nb<sub>6</sub>Co<sub>7</sub> (Figure S6a, Supporting Information) and  $\mu$ -Nb<sub>7</sub>Co<sub>6</sub> (Figure S6b, Supporting Information) both vanish due to the large prestrain. According to the NEB calculations, the associated atomic mechanisms of basal slip on  $P_{t-k}$  in  $\mu$ -Nb<sub>6</sub>Co<sub>7</sub> and  $\mu$ -Nb<sub>7</sub>Co<sub>6</sub> are different. The intermediate states of the basal slip on  $P_{t-k}$  in  $\mu$ -Nb<sub>6</sub>Co<sub>7</sub> (Figure 4e) show that basal slip on  $P_{t-k}$  in  $\mu$ -Nb<sub>6</sub>Co<sub>7</sub> occurs via a crystallographic slip mechanism along the  $\frac{1}{3}\langle 11\bar{2}0 \rangle$  direction. The triple layer moves as a whole along the  $\frac{1}{3}\langle 11\bar{2}0 \rangle$  direction relative to the kagomé layer above. The stacking sequence of the triple layer in  $\mu$ -Nb<sub>6</sub>Co<sub>7</sub> therefore remains unchanged during the glide process. However, the intermediate states of basal slip on  $P_{t-k}$  in  $\mu$ -Nb<sub>7</sub>Co<sub>6</sub> (Figure 4f) show that basal slip on  $P_{t-k}$  in  $\mu$ -Nb<sub>7</sub>Co<sub>6</sub> occurs via a glide and shuffle mechanism. An out-of-plane atomic shuffling between the top and the middle of the triple layer occurs during the glide process on the  $P_{t-k}$  plane along the  $\langle \bar{1}100 \rangle$  direction. The Nb atoms on the top move to the middle of the triple layer, and meanwhile the Nb atoms in the middle adjust their positions to the top of the triple layer. After the glide and shuffle process, the triple layer changes to the twinned variant, and a stable stacking fault with a low stacking fault energy of 7.6 mJ m<sup>-2</sup> is created. The configuration of the stacking fault is consistent with those widely observed in the HAADF-STEM images of  $\mu$ -Nb<sub>7</sub>Co<sub>6</sub> (Figure 3c). Although in  $\mu$ -Nb<sub>7</sub>Co<sub>6</sub> the configuration and the associated stacking fault energy of this type of stacking fault are the same as the stacking fault created by synchroshear, the stacking faults in the Nb<sub>7</sub>Co<sub>6</sub> alloy are more likely to be created

by the glide and shuffle mechanism rather than the synchroshear mechanism due to the high energy barrier to synchroshear. However, this type of stacking fault created by the glide and shuffle mechanism is unlikely to occur in C15–NbCo<sub>2</sub> and  $\mu$ -Nb<sub>6</sub>Co<sub>7</sub> since it disrupts the stable Nb–Co–Nb configuration of the triple layer (Figure S7, Supporting Information), and thus the energy of this type of stacking fault is very high in C15–NbCo<sub>2</sub> (802.1 mJ m<sup>-2</sup>) and  $\mu$ -Nb<sub>6</sub>Co<sub>7</sub> (471.7 mJ m<sup>-2</sup>) (Table S4, Supporting Information). Although the Nb<sub>6.4</sub>Co<sub>6.6</sub> alloy mainly deforms by full dislocation slip on  $P_{t-k}$ , given that nearly 43.5% of the Co atoms in the middle of the triple layers are replaced by Nb atoms at 49.5 at% Nb, the energy of the stacking fault created by the glide and shuffle mechanism might be reduced, and thus the full dislocations might be able to dissociate with the help of local fluctuations in composition.

### 3. Conclusion

We can now interpret the plasticity of the Nb–Co  $\mu$ -phase by elucidating the influences of crystal structure and composition on the mechanical behavior of the Laves phase building block. As the crystal structure changes from the C15–NbCo<sub>2</sub> Laves phase to the Nb–Co  $\mu$ -phase, the interplanar spacing  $d_t$  decreases and the interplanar spacing  $d_{t-k}$  increases. As a result of the changes in interplanar spacings of the Laves phase building block, the energy barrier to synchroshear dramatically increases, whereas the energy barrier to basal slip between the triple layer and kagomé layer decreases. Thus, the basal slip mechanism tends to change from synchroshear in the C15–NbCo<sub>2</sub> to basal slip between the triple layer and kagomé layer in the Nb–Co  $\mu$ -phase. The excess Nb atoms in the Nb-rich Nb–Co  $\mu$ -phase are accommodated by the site specific substitutions of the Co atoms in the triple layer of the NbCo<sub>2</sub> Laves phase building block. As the composition changes from Nb<sub>6</sub>Co<sub>7</sub> to Nb<sub>7</sub>Co<sub>6</sub>, the Nb–Co–Nb triple layer becomes a slab of pure Nb, resulting in a reduction in stiffness, especially the basal plane shear modulus of the NbCo<sub>2</sub> Laves phase building block, and an increased elastic inhomogeneity between the Nb<sub>4</sub>Co<sub>3</sub> and NbCo<sub>2</sub> Laves phase building blocks. The changes in the atomic configurations of the NbCo<sub>2</sub> Laves phase building block also lead to a reduction in energy barrier to basal slip on the  $P_{t-k}$  plane and formation of stable stacking faults via the glide and shuffle mechanism. Therefore, as the composition of the Nb–Co  $\mu$ -phase changes from Nb<sub>6</sub>Co<sub>7</sub> to Nb<sub>7</sub>Co<sub>6</sub>, basal slip on the  $P_{t-k}$  plane becomes easier and a transition of basal slip mechanism from the crystallographic slip to the glide and shuffle mechanism occurs.

The strong influence of the structure and chemical composition on the mechanical behavior of the Laves phase building block sheds light on how to control the mechanical properties of the complex  $\mu$ -phase. It therefore opens up opportunities to make the hard and brittle  $\mu$ -phase phases much softer and deformable at even ambient temperature.<sup>[17]</sup> In highly alloyed systems, such as superalloys, high temperature steels, or high entropy alloys, which are prone to  $\mu$ -phase precipitation, this understanding may be employed directly by selecting alloying elements that lead to the formation of  $\mu$ -phases with a soft triple layer occupied by the same or similarly sized metallic species only and a corresponding large spacing between triple and kagomé layer.<sup>[18]</sup>



Similarly, where alloying elements cannot be selected on this basis, the often-available high resolution chemical information on precipitates may now be used to estimate relative hardness of precipitates that remain too small for quantitative mechanical testing. The structural and chemical data may then give an indication of whether or not the present precipitates are likely to later introduce local damage in the microstructure or not.

Furthermore, these insights also have implications for understanding of the plasticity of complex intermetallic phases with a layered structure in general. The plasticity of the complex intermetallic phases built from layers of recurring building blocks, such as ternary transition metal nitrides/carbides (MAX phases),<sup>[19]</sup> can be governed by the mechanisms active in the fundamental subunits and may be tailored by tuning local bonding conditions and lattice spacing. To study the interplay of interplanar spacing, local shear modulus and plasticity in the recurrent fundamental building blocks will also allow us to transfer our understanding of their deformation to a large number of complex intermetallic phases that may be newly considered or discovered for the development of new high performance materials.

#### 4. Experimental Section

**Preparation of Samples:** Nb<sub>6.4</sub>Co<sub>6.6</sub>, Nb<sub>6.9</sub>Co<sub>6.1</sub>, and Nb<sub>7</sub>Co<sub>6</sub> alloys of the Nb–Co  $\mu$ -phase were prepared from pure Co (99.98 wt%) and Nb (99.9 wt%) by arc melting in an argon atmosphere. To assure homogeneity, all samples were turned over and remelted 5 times. The alloys were heat-treated at 1150 °C for 500 h under high vacuum. The ingots were cut into small disks with a thickness of 2 mm and a diameter of 8 mm, mechanically ground, and polished using an OP-U (Struers GmbH) finish. The microstructures of the alloys were observed by optical microscopy (Leica DMR, Leica AG) and SEM (Helios Nanolab 600i, FEI). Electron backscatter diffraction (EBSD) (Hikari, EDAX) measurements were performed to determine the crystallographic grain orientations. The electron probe microanalysis (JXA-8530F, JEOL) was performed to determine the chemical compositions and homogeneity of the alloys (Figure S4, Supporting Information) using pure Co and Nb as standards. Three line scans in different areas far away from each other were measured on each alloy. Each line scan contained 11 spot analyses. The Nb<sub>6.4</sub>Co<sub>6.6</sub>, Nb<sub>6.9</sub>Co<sub>6.1</sub>, and Nb<sub>7</sub>Co<sub>6</sub> alloys were homogeneous and their average compositions were 49.5 ± 0.2, 52.8 ± 0.1, 53.7 ± 0.2 at% Nb, respectively.

**Nanoindentation Tests:** Nanoindentation tests were carried out at room temperature using a Nanomechanics iNano indenter equipped with a continuous stiffness measurement (CSM) unit. The samples were indented using a diamond Berkovich indenter tip up to a maximum load of 45 mN. The strain rate was kept constant at 0.002 s<sup>-1</sup> and the maximum load was held for 10 s before unloading. The CSM method allowed continuous measurements of hardness and indentation modulus as a function of indentation depth using the model and methods proposed by Phani et al.<sup>[20]</sup> To minimize the indentation size effect, the hardness and indentation modulus were obtained by averaging the values measured at an indentation depth greater than 350 nm. The macroscopic hardness was estimated following the model proposed by Nix and Gao<sup>[15]</sup> and using the indentation depth and hardness data above 200 nm. From this indentation depth, the Nix–Gao plot of hardness squared versus the inverse indentation depth yielded the expected, approximately linear relationship, as observed for MgO as a similarly hard material.<sup>[21]</sup> A minimum of 220 indentation tests were performed in each alloy. The indents were at least 50  $\mu$ m from visible cracks and 20  $\mu$ m from consecutive indents. After indentation tests, the indents were imaged by SEM and the indents in the vicinity of cracks and pores were excluded from the analysis. The indents selected for slip traces analysis were further examined by EBSD to facilitate a correlation of surface morphology and crystal orientation.

**TEM Investigations:** In order to verify the activated slip systems and reveal the detailed dislocation mechanisms of the plasticity of the Nb–Co  $\mu$ -phase, TEM investigations on the dislocation structures of the Nb<sub>6.4</sub>Co<sub>6.6</sub> and Nb<sub>7</sub>Co<sub>6</sub> alloys were performed after indentation tests. Specimens for TEM analysis were prepared from selected indents of the Nb<sub>6.4</sub>Co<sub>6.6</sub> and Nb<sub>7</sub>Co<sub>6</sub> alloys by focused ion beam (FIB) milling (Helios Nanolab 600i, FEI). TEM observations were carried out with a JEOL JEM F200 electron microscope operated at 200 kV and two probe-corrected scanning TEMs (a Thermo Fisher Scientific Spectra Ultra S/TEM equipped with the Ultra X EDS solution, and a Titan Themis) operated at 300 kV. EDS spectrum imaging was obtained at 300 kV and noise reduction was performed using multivariate statistical analysis.<sup>[22]</sup>

**DFT Calculations:** DFT calculations were carried out using the Quantum ESPRESSO<sup>[23]</sup> package with the projector augmented wave<sup>[24]</sup> method and the Perdew–Burke–Ernzerhof<sup>[25]</sup> generalized gradient approximation to the exchange correlation functional. The kinetic energy cutoff was 60 Ry for wave functions and 360 Ry for charge densities and potentials. The convergence threshold for electronic self-consistency was 10<sup>-8</sup> Ry. The Broyden–Fletcher–Goldfarb–Shanno<sup>[26]</sup> relaxation scheme was used for structural relaxation, the convergence thresholds of energy and force were 10<sup>-4</sup> and 2 × 10<sup>-4</sup> au (atomic units), respectively. The conventional unit cells with an 8 × 8 × 1 *k*-point mesh (for  $\mu$ -Nb<sub>6</sub>Co<sub>7</sub> and  $\mu$ -Nb<sub>7</sub>Co<sub>6</sub>) and 1 × 1 × 2 unit cells with a 5 × 5 × 3 *k*-point mesh (for C15–NbCo<sub>2</sub>) were used to calculate the lattice parameters and elastic properties. The local shear moduli of crystal building blocks were calculated following the method introduced by Howie et al.<sup>[19]</sup> For the GSF and climbing image NEB<sup>[27]</sup> calculations, the simulation cells were 1 × 1 × 2 unit cells (for  $\mu$ -Nb<sub>6</sub>Co<sub>7</sub> and  $\mu$ -Nb<sub>7</sub>Co<sub>6</sub>) and 1 × 1 × 13 unit cells (for C15–NbCo<sub>2</sub>) with a 6 × 6 × 1 or 8 × 8 × 1 *k*-point mesh. The periodic boundary conditions (PBC) and perpendicular relaxation suggested by Rodney et al.<sup>[28]</sup> were applied during the rigid body shift of the GSF calculations (Figure S5a, Supporting Information). For the NEB calculations, the initial and final images as well as the interpolated intermediate images were presheared to retain the PBC in the longitudinal direction (Figure S5b, Supporting Information). The Quickmin method<sup>[29]</sup> was used to minimize the energies across all images with a force tolerance of 0.05 eV Å<sup>-1</sup>. The spring constant for nudging force was 0.1 au. 7 or 14 intermediate images were used, and all images were equally spaced along the reaction coordinate. The Open Visualization Tool (OVITO)<sup>[30]</sup> was used to visualize the atomistic configurations and trajectories of atoms.

#### Supporting Information

Supporting Information is available from the Wiley Online Library or from the author.

#### Acknowledgements

The authors thank Dunming Wu, David Beckers, and Arndt Ziemons for their help in sample preparation, Martin Heller and Risheng Pei for their help in focused ion beam milling, James Best for the help in nanoindentation, Stefanie Sandlöbes-Haut for fruitful discussions, and Mattis Seehaus for his help during the revision of this paper. This project has received funding from the European Research Council (ERC) under the European Union's Horizon 2020 Research and Innovation Programme (Grant Agreement No. 852096 FunBlocks). Funding by the Deutsche Forschungsgemeinschaft (DFG) in Projects KO 4603/2-2 (Project ID 437514011) and SFB1394 Structural and chemical atomic complexity – from defect phase diagrams to material properties (Project ID 409476157) is gratefully acknowledged. Simulations were performed with computing resources granted by the RWTH Aachen University under Project (No. p0020267). The authors would also like to thank the anonymous reviewers for their very detailed and constructive comments.

Open access funding enabled and organized by Projekt DEAL.

## Conflict of Interest

The authors declare no conflict of interest.

## Data Availability Statement

The data that support the findings of this study are available from the corresponding author upon reasonable request.

## Keywords

dislocations, intermetallics, Laves phase building blocks, Nb–Co alloys, plasticity

Received: January 18, 2023

Revised: March 3, 2023

Published online:

- [1] C. C. Tasan, M. Diehl, D. Yan, M. Bechtold, F. Roters, L. Schemmann, C. Zheng, N. Peranio, D. Ponge, M. Koyama, *Annu. Rev. Mater. Res.* **2015**, *45*, 391.
- [2] a) R. Fleischer, D. Dimiduk, H. Lipsitt, *Annu. Rev. Mater. Sci.* **1989**, *19*, 231; b) G. Sauthoff, *Intermetallics* **2000**, *8*, 1101.
- [3] a) E. Parthe, L. Gelato, B. Chabot, M. Penzo, K. Cenzual, R. Gladyshevskii, *TYPIX-Standardized Data and Crystal Chemical Characterization of Inorganic Structure Types*, Springer, Berlin, Germany **1993**; b) B. C. E. Parthé, K. Cenzual, *Chimia* **1985**, *39*, 164.
- [4] a) C. M. F. Rae, R. C. Reed, *Acta Mater.* **2001**, *49*, 4113; b) B. Seiser, R. Drautz, D. G. Pettifor, *Acta Mater.* **2011**, *59*, 749.
- [5] K. S. Kumar, P. M. Hazzledine, *Intermetallics* **2004**, *12*, 763.
- [6] a) P. M. Hazzledine, P. Pirouz, *Scr. Metall.* **1993**, *28*, 1277; b) M. F. Chisholm, S. Kumar, P. Hazzledine, *Science* **2005**, *307*, 701.
- [7] a) O. Vedmedenko, F. Rösch, C. Elsässer, *Acta Mater.* **2008**, *56*, 4984; b) W. Zhang, R. Yu, K. Du, Z. Cheng, J. Zhu, H. Ye, *Phys. Rev. Lett.* **2011**, *106*, 165505; c) J. Guérolé, F.-Z. Mouhib, L. Huber, B. Grabowski, S. Korte-Kerzel, *Scr. Mater.* **2019**, *166*, 134.
- [8] a) Z. Xie, D. Chauraud, A. Atila, E. Bitzek, S. Korte-Kerzel, J. Guérolé, **2022**, arXiv: 2205.02669; b) A. V. Kazantzis, M. Aindow, G. K. Triantafyllidis, J. T. M. De Hosson, *Scr. Mater.* **2008**, *59*, 788; c) A. V. Kazantzis, M. Aindow, I. P. Jones, G. K. Triantafyllidis, J. T. M. De Hosson, *Acta Mater.* **2007**, *55*, 1873.
- [9] a) R. Darolia, D. Lahrman, R. Field, in *Superalloys 1988* (Eds: D. N. Duhl, G. Maurer, S. Antolovich, C. Lund, S. Reichman), Champion, Alexandria, VA, USA **1988**; b) J. Zhu, H. Q. Ye, *Scr. Metall. Mater.* **1990**, *24*, 1861.
- [10] A. K. Sinha, *Prog. Mater. Sci.* **1972**, *15*, 81.
- [11] a) S. Schröders, S. Sandlöbes, C. Birke, M. Loeck, L. Peters, C. Thomas, S. Korte-Kerzel, *Int. J. Plast.* **2018**, *108*, 125; b) S. Schröders, S. Sandlöbes, B. Berkels, S. Korte-Kerzel, *Acta Mater.* **2019**, *167*, 257.
- [12] V. Wagner, M. Conrad, B. Harbrecht, *Acta Crystallogr. C* **1995**, *51*, 1241.
- [13] N. Mevenkamp, B. Berkels, in *Pattern Recognition, DAGM 2015, Lecture Notes in Computer Science* (Eds: J. Gall, P. Gehler, B. Leibe), Vol. 9358, Springer, Cham, Switzerland **2015**.
- [14] a) W. Luo, C. Kirchlechner, J. Zavašnik, W. Lu, G. Dehm, F. Stein, *Acta Mater.* **2020**, *184*, 151; b) C. Zehnder, K. Czerwinski, K. D. Molodov, S. Sandlöbes-Haut, J. S. K. L. Gibson, S. Korte-Kerzel, *Mater. Sci. Eng., A* **2019**, *759*, 754.
- [15] W. D. Nix, H. Gao, *J. Mech. Phys. Solids* **1998**, *46*, 411.
- [16] W. Luo, Z. Xie, P. L. Sun, J. S. K. L. Gibson, S. Korte-Kerzel, *Acta Mater.* **2023**, *246*, 118720.
- [17] a) J. X. Yang, Q. Zheng, X. F. Sun, H. R. Guan, Z. Q. Hu, *Scr. Mater.* **2006**, *55*, 331; b) M. Simonetti, P. Caron, *Mater. Sci. Eng., A* **1998**, *254*, 1; c) M. Pessah, P. Caron, T. Khan, in *Superalloys 1992* (Eds: S. D. Antolovich, R. W. Stusrud, R. A. MacKay, D. L. Anton, T. Khan, R. D. Kissinger, D. L. Klarstrom), Champion, Alexandria, VA, USA **1992**.
- [18] X. Wu, W. Liu, X.-G. Lu, Y. Jiang, Y. He, *J. Solid State Chem.* **2022**, *305*, 122704.
- [19] P. R. Howie, R. P. Thompson, S. Korte-Kerzel, W. J. Clegg, *Sci. Rep.* **2017**, *7*, 11602.
- [20] a) P. S. Phani, W. C. Oliver, G. M. Pharr, *J. Mater. Res.* **2021**, *36*, 2137; b) W. C. Oliver, G. M. Pharr, *J. Mater. Res.* **2004**, *19*, 3.
- [21] G. Feng, W. D. Nix, *Scr. Mater.* **2004**, *51*, 599.
- [22] S. Zhang, C. Scheu, *Microscopy* **2018**, *67*, i133.
- [23] a) P. Giannozzi, S. Baroni, N. Bonini, M. Calandra, R. Car, C. Cavazzoni, D. Ceresoli, G. L. Chiarotti, M. Cococcioni, I. Dabo, A. Dal Corso, S. de Gironcoli, S. Fabris, G. Fratesi, R. Gebauer, U. Gerstmann, C. Gougoussis, A. Kokalj, M. Lazzeri, L. Martin-Samos, N. Marzari, F. Mauri, R. Mazzarello, S. Paolini, A. Pasquarello, L. Paulatto, C. Sbraccia, S. Scandolo, G. Sclauzero, A. P. Seitsonen, et al., *J. Phys.: Condens. Matter* **2009**, *21*, 395502; b) P. Giannozzi, O. Andreussi, T. Brumme, O. Bunau, M. Buongiorno Nardelli, M. Calandra, R. Car, C. Cavazzoni, D. Ceresoli, M. Cococcioni, N. Colonna, I. Carnimeo, A. Dal Corso, S. de Gironcoli, P. Delugas, R. A. DiStasio, A. Ferretti, A. Floris, G. Fratesi, G. Fugallo, R. Gebauer, U. Gerstmann, F. Giustino, T. Gorni, J. Jia, M. Kawamura, H. Y. Ko, A. Kokalj, E. Küçükbenli, M. Lazzeri, et al., *J. Phys.: Condens. Matter* **2017**, *29*, 465901.
- [24] a) P. E. Blöchl, *Phys. Rev. B* **1994**, *50*, 17953; b) G. Kresse, D. Joubert, *Phys. Rev. B* **1999**, *59*, 1758.
- [25] J. P. Perdew, K. Burke, M. Ernzerhof, *Phys. Rev. Lett.* **1996**, *77*, 3865.
- [26] R. Fletcher, *Practical Methods of Optimization*, John Wiley & Sons, Hoboken, NJ, USA **2013**.
- [27] a) G. Henkelman, B. P. Uberuaga, H. Jónsson, *J. Chem. Phys.* **2000**, *113*, 9901; b) G. Henkelman, H. Jónsson, *J. Chem. Phys.* **2000**, *113*, 9978.
- [28] D. Rodney, L. Ventelon, E. Clouet, L. Pizzagalli, F. Willaime, *Acta Mater.* **2017**, *124*, 633.
- [29] D. Sheppard, R. Terrell, G. Henkelman, *J. Chem. Phys.* **2008**, *128*, 134106.
- [30] A. Stukowski, *Modell. Simul. Mater. Sci. Eng.* **2010**, *18*, 015012.